Article

Not peer-reviewed version

Tuning of structural, morphological and optical properties of PA 6 upon stepwise insertion of amorphous Se, Cd2+ and Ag+ ions

Emilija Skuodaitė and Valentina Krylova *

Posted Date: 6 July 2023

doi: 10.20944/preprints202307.0328.v1

Keywords: polyamide 6; selenium; cadmium; silver; selenides; nanofilms; optical properties; light-absorbing materials

Article

Tuning of Structural, Morphological and Optical Properties of PA 6 upon Stepwise Insertion of Amorphous Se, Cd^{2+} and Ag^{+} Ions

Emilija Skuodaitė and Valentina Krylova *

Department of Physical and Inorganic Chemistry, Faculty of Chemical Technology, Kaunas University of Technology, Radvilėnų Str. 19, 50254 Kaunas, Lithuania; emilija.skuodaite@ktu.edu

* Correspondence: valentina.krylova@ktu.lt

Abstract: Increasing photon absorption by capturing light is an important way to increase the efficiency of photovoltaic devices. In this regard, the small optical band gap (E_g) and high absorption coefficient of Se-containing thin nanofilms make them ideal for next generation photovoltaic devices based on selenides. This study reports on chemical synthesis processes in a bath for the insertion of amorphous selenium into polyamide-6 (PA 6) matrix and the effect of incorporation of Cd^{2+} and Ag^{+} on the structural, morphological and optical properties. The resulting films had a pyramidal structure of single crystals, nanosized particles of nonspecific shape, agglomerated and indistinct grains. ATR-FTIR spectroscopy revealed the interaction between PA 6 and inorganic components, which causes obvious conformational changes in PA 6 chains. The data of X-ray diffraction analysis, depending on the stage of synthesis, showed a mixture of various compounds: Se_8, CdSe, Ag_2Se and Ag. This may explain the observed optical properties. The optical properties of the composites indicate a shift in the band gap from 4.46 eV for PA 6 to 2.23-1.64 eV upon stepwise insertion of amorphous Se, Cd^{2+} and Ag^{+} ions. E_g is conveniently located in the visible region of solar energy, making the obtained nanofilms ideal for solar energy harvesting.

Keywords: polyamide 6; selenium; cadmium; silver; selenides; nanofilms; optical properties; light-absorbing materials

1. Introduction

Nanoscale sized inorganic materials within the polymers are interesting in optoelectronics as light emitting devices [1] or photovoltaics [2], separation-catalysis [3] and bioelectronics [4]. The semiconductor nanoparticles embedded in the polymer film are easy to process [5]. These composites are usually made by mixing inorganic and organic components, and the obtained structure has physical and chemical properties that are not present in the individual components [1].

Selenium and selenium-containing materials have become the subject of many scientific studies due to their exceptional physical-chemical properties and photoelectric characteristics [6–8]. As an important inorganic material, selenium has also received a lot of attention due to its good semiconductor properties. For an a-Se film with a thickness of 4200 Å, the value of the band gap is 1.76 eV [9,10]. Due to their high photoconductivity, various selenides are one of the key materials widely used in optoelectronic devices such as photocopiers, light emitting diodes, xerography, and solar cells [8,11–13].

Doping with impurity atoms is an effective strategy for optimising the properties required for the development of semiconductor technologies. Newly developed aliovalent doping provides extra electrons (n-type doping) or extra holes (p-type doping) to redefine their doping type for electronic requirements. For CdSe, the most studied nanocrystalline system, it has been proved that additional carriers from heterovalent dopants such as Ag, Cu and In [14,15] can enhance the electronic conductivity in films when they are excited by external energy. Incorporating aliovalent metal cations into binary, such as CdSe, semiconductors change the optoelectronic properties of the

 doi:10.20944/preprints202307.0328.v1

newly formed base material, providing greater performance in a number of applications, including solar cells, batteries, and LEDs [16–18].

Polyamides are widely used as technical polymers with applications ranging from synthetic fibres to industrial and structural applications. Typically, optoelectronic devices use a combination of highly conductive semiconductor components due to their electrical pumping capability and the strong interaction of light and matter of the organic component [19]. The efficient inorganic materials used include cadmium selenide (CdSe) [11] and silver selenide (Ag_2Se) [12,13]. CdSe and Ag_2Se are direct bandgap semiconducting materials with the corresponding bandgaps of 1.9 eV [20] and 1.8 eV [21], respectively.

Due to the high reduction potential of Se(IV)/Se(0), various reagents for reduction of selenium (IV) compounds in several types of aqueous solutions have been evaluated. N_2H_4 [6,22], $(NH_2)_2CS$ [23], metallic Fe or Zn [24–27], CuCl [28], $TiCl_3$ [29**], $SnCl_2$ [30**], $Na_2S_2O_4$ [31], *D*-fructose [32], and ascorbic acid [33] have been proposed as quantitative reducing agents for Se(IV) in acidic solutions. In industrial applications, SO_2 is the preferred reagent for the reduction of Se(IV) to its elemental state. According to literature data [10,34], when working with hot (>80 °C) and relatively concentrated solutions of H_2SO_4 or HCl (pH <1), the complete reduction of selenium occurs very quickly. However, high toxicity (hydrazine and thiourea), low efficiency (zinc, *D*-fructose, ascorbic acid) and high cost (CuCl, $TiCl_3$, $Na_2S_2O_4$ and $SnCl_2$) limit the applicability of these reagents. The better candidate for this purpose as a strong reducing agent is sodium sulphite (Na_2SO_3), because of its fast reaction rate, low cost, and relatively low toxicity.

Solution-based chemical methods provide an excellent way to produce nano selenium and nano selenides. Each synthesis method has its own advantages in obtaining the appropriate structures and properties for each system, and hence the right combinations of processing along with suitable systems must be found to achieve the desired goal.

This work is aimed at studying the change in the properties of PA6 upon the stepwise introduction of amorphous Se, Cd^{2+} and Ag^{+} ions and understanding the factors that determine the properties of these light-absorbing materials. These composites in the PA6 membrane were prepared using various chemical synthesis methods: Se—by chemical bath deposition (CBD), Cd^{2+} and Ag^{+} selenide—by successive ionic layer adsorption and reaction (SILAR), and mixed Ag^{+}-Cd^{2+} selenide composites were prepared using cation exchange (CE). For a deeper understanding of the relationship between the composition and consumer properties of polyamide-6-based selenium nanocomposites, the main attention was paid to the description of the microstructure, morphology, and physicochemical properties.

2. Materials and Methods

Semicrystalline flexible TECAMID®6 (polyamide 6, PA 6) produced by Ensinger GmbH (Germany) was used as a thermoplastic matrix. Nominal characteristics provided by the manufacturer are: PA 6 film was opaque, 0.5 mm thick, density 1.13 g/cm^3, moisture absorption 3 %, water absorption to equilibrium 9.5 %. Experiments were performed on 2′6 cm^2 cuts in a film. Prior to the experiments, PA 6 film cuts were washed with $NaHCO_3$ and heated in distilled water for 2 h at 100°C to remove surface contamination. The criterion for the quality treatment of the PA 6 substrate surface was its uniform wetting with distilled water. After treatment, the substrates were stored in a desiccator.

Selenious acid (H_2SeO_3, 99.0%), sodium sulphite heptahydrate ($Na_2SO_3 \cdot 7H_2O$, 99.0%), sulphur acid (H_2SO_4, 96%), cadmium nitrate tetrahydrate ($Cd(NO_3)_2 \cdot 4H_2O$, 99.997% trace metals basis), silver nitrate ($AgNO_3$, 99.0%) were purchased from Aldrich Chemical Co and used as received. All solutions were prepared using distilled water.

The first step involved the synthesis of Se via the CBD process. For Se deposition/insertion, the cleaned PA 6 films cuts were vertically immersed into a beaker with 0.1 M H_2SeO_3 and 0.15 M Na_2SO_3 solutions and exposed in a thermostatic vessel for 24 h at 20±1 °C. The concentrations of the H_2SeO_3 and Na_2SO_3 solutions (pH 2 with the addition of H_2SO_4), the deposition temperature and exposure time were chosen to give excellent composites in terms of continuity, smoothness and

Preprints (www.preprints.org) | NOT PEER-REVIEWED | Posted: 6 July 2023 doi:10.20944/preprints202307.0328.v1

adhesion to the substrate. The solution was clear at first, became slightly turbid after two hours and turned into a light red liquid after a few hours. The Se precipitate was very fine, but it aggregated into large clusters within ~24 h. This proposed mechanism for the formation of Se films is based on nucleation and the Ostwald ripening process [35]. This process is simple, controllable and reproducible. After deposition/insertion of the Se, the upper layer (Figure 1) was removed from the PA6 surface with filter paper, samples were thoroughly washed with distilled water, and stored in a desiccator between the individual processing steps. Then obtained composites (in the text referred to as a-Se/PA 6) were used as the initial composite for the stepwise insertion of Cd^{2+} and Ag^{+} ions. For this, half of the a-Se/PA6 composites were treated for 3 h with a 0.1 M solution of $Cd(NO_3)_2$ (pH 5.4) at a temperature of 80±1 °C. The second half of a-Se/PA6 composites were treated for 2 h with a 0.1 M solution of $AgNO_3$ (pH 6.35) at a temperature of 20±1 °C. The obtained composites were labelled as Cd-Se/PA 6 and Ag-Se/PA 6, respectively. Then one part of the Cd-Se/PA 6 composites were treated for 10 min with a 0.05 M $AgNO_3$ solution (pH 6.45, temperature of 20±1 °C) and washed well as described above. After immersion in the $AgNO_3$ solution, the resulting composites (throughout the text labelled as Ag-Cd-Se/PA 6) were black uniform and highly reflective with good adhesion. In all cases samples were treated in a thermostated vessel. During the deposition process, the beaker was kept undisturbed. All deposited films were evaluated for adhesion by subjecting them to a steady stream of distilled water. After each deposition step, the samples were washed first with hot and then cold distilled water, dried at ambient temperature, and stored in a desiccator until analysis. Figure 1 shows schematic outline of the approach and optical micrographs image of PA 6 membrane and obtained composites.

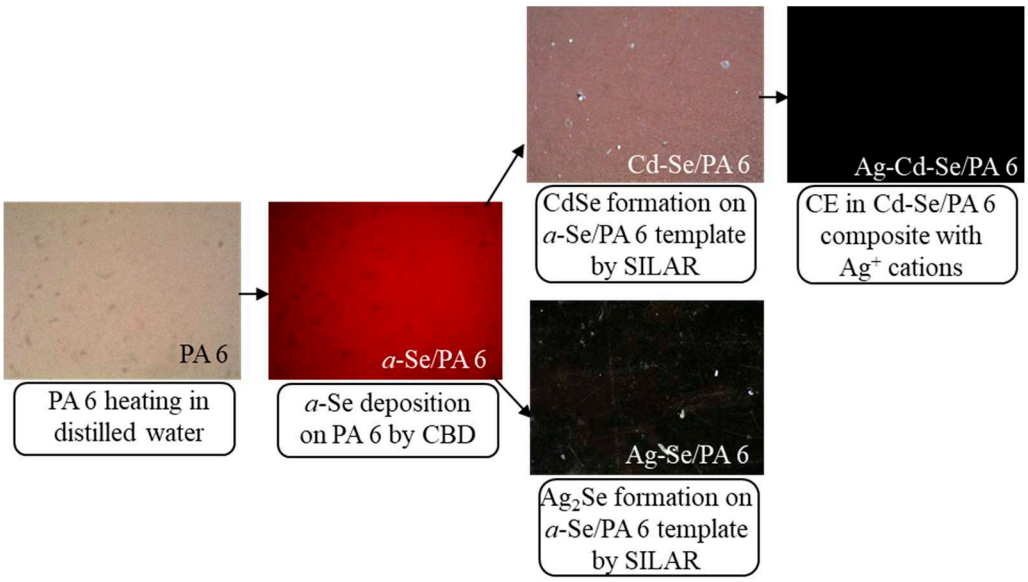

Figure 1. The principal route of combined CBD, SILAR and CE methods for the Se, Cd^{2+} and Ag^{+} deposition/insertion in PA 6 membrane. Above optical micrographs image of the PA 6 membrane and obtained composites. Magnification ×100.

The porosity of the PA 6 film samples was measured by the BET (abbreviated from Brunauer-Emmett-Teller theory) method using nitrogen adsorption porosimeter Nova 2200 E-Series (Quantachrome Instruments, Boynton Beach, FL, USA). Before analysis, the film samples were degassed under vacuum at 100 °C.

Solution pH was measured using a pH-meter WTW330 (WTW GmbH, Weilheim, Germany). Optical microscopy images were obtained using an Olympus CX31 optical microscope and a C-5050 camera (Japan).

The structure of the composites was analysed using X-ray diffraction method (XRD) on a Bruker Advance D8 diffractometer. The XRD patterns were produced with CuKα (λ = 0.154178 nm)

Preprints (www.preprints.org) | NOT PEER-REVIEWED | Posted: 6 July 2023 doi:10.20944/preprints202307.0328.v1

radiation in the 2θ scanning mode. The XRD data were analysed by observing characteristic peaks in the X-ray diffraction patterns using Search Match software and PDF-2 and PDF-4 database. Crystallite size (D_c) values were calculated from XRD patterns based on Bragg and Scherrer equation [36]:

$$D_C = \frac{K\lambda}{\beta(2\theta)\cos\theta}1, \quad (1)$$

where K—constant with a normal value of 0.89, λ –wavelength of CuKα radiation, $\beta(2\theta)$ represents the full width at the half-maximum, and θ—Bragg angle. The dislocation density (δ) was evaluated by using the equation [37]:

$$\delta = \frac{1}{D^2}, \text{ (line·m}^{-2}), \quad (2)$$

The strain values (ε) were calculated from the following relation:

$$\varepsilon = \frac{\beta\cos\theta}{4} \text{ (line}^{-2}\text{·m}^{-4}), \quad (3)$$

Surface topography imaging was conducted using atomic force microscopy (AFM) using a NanoWizard®3 NanoScience microscope, data were analysed using JPKSPM Data Processing software. The AFM images (scanning area 5×5 μm²) were collected using an AppNano production pyramidal-shaped i-type silicon cantilever (0.01–0.025 ohm/cm, spring constant of 2 N/m) working in contact mode.

Ultraviolet-visible (UV-Vis) absorption spectra (200 to 1100 nm) were recorded on a Spectronic Genesys 8 UV-Vis spectrophotometer with compensation for PA6 absorption. The energy optical band gaps (E_g) were determined by applying the absorption spectrum fitting method [38]. The fundamental absorption edge (λ_g) can be found from the plot:

$$\left(\frac{A}{\lambda}\right)^{1/m} = f\frac{1}{\lambda}, \quad (4)$$

where A—absorption, λ—wavelength, m—index which takes values 0.5, 1.5, 2 and 3 for direct allowed, direct forbidden, indirect allowed and indirect forbidden transitions, respectively. Extrapolating of straight-line portion to cut the energy axis gives λ_g. Then employing the obtained value of λ_g the E_g can be directly calculated from the following relation [38]:

$$E_g = \frac{1239.83}{\lambda_g}, \quad (5)$$

The Urbach energy (E_U) is related to the absorption coefficient by the following exponential equation [39]:

$$\alpha = \alpha_0 \cdot e^{h\nu/E_U}, \quad (6)$$

E_U was calculated using the slope determined from the linear part of the plot between ln(A) versus $1/\lambda$ according to the following relation:

$$E_U \cdot tg\alpha = 1239.83, \quad (7)$$

The steepness parameter σ is related with E_U the by following equation:

$$\sigma = \frac{k\cdot T}{E_U}, \quad (8)$$

where k is the Boltzmann constant, $8.617343\cdot10^{-5}$ eV/K and T the absolute temperature assumed to be 298 K. The following equation is applied for calculating the interaction strength of electron–phonon ($E_{e\text{-}p}$) [40]:

$$Ee\text{–}p = 23\sigma, \quad (9)$$

The optical electronegativity χ is related with E_g by following equation:

$$\chi = 2.688 \cdot E_g, \quad (10)$$

Preprints (www.preprints.org) | NOT PEER-REVIEWED | Posted: 6 July 2023 doi:10.20944/preprints202307.0328.v1

The changes in the chemical structure and the binding configuration of the samples were analysed using attenuated total reflectance (ATR) Fourier transform infra-red spectroscopy (FTIR). The ATR-FTIR spectra were recorded on a Perkin Elmer FT-IR Spectrum GX system (Perkin Elmer, Waltham, MA, USA) in the wavenumber range 4000–600 cm^{-1}. Spectra were recorded by averaging 64 scans with a wavenumber resolution of 1 cm^{-1} at room temperature

3. Results and Discussions

Adsorption membranes are one of the best ways to obtain semiconductor composites from aqueous solutions. The established pore size less than 2 nm indicates that the PA 6 film is microporous. Therefore, it can adsorb Se micro particles and Cd^{2+} and Ag^{+} cations followed by their diffusion into the polymer membrane. In most cases, adsorption membranes are charged. There is an attraction of charges between the ions and the surface of the adsorption membrane.

3.1. XRD Analysis

To determine the structural properties of the PA 6 and the obtained composites, XRD patterns were analysed. The XRD pattern of PA 6 sample heated in distilled water is shown in Figures 2 and 4, while XDR pattern of the obtained composites is shown in Figure 4.

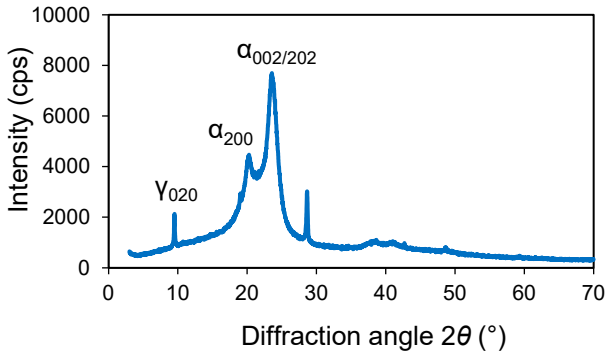

Figure 2. XRD pattern of the PA 6 sample heated in distilled water.

PA 6 crystallizes into stable α- and γ-, as well as unstable β-forms [41]. XRD studies of the PA 6 sample revealed the presence of a main peaks at 2θ 9.52°, 20.26°, 23.56° and 28.64°. The small diffraction peak at 2θ = 9.52°, which was attributed to the (020) reflection of the γ crystalline form [40]. The other two peaks at 2θ = 20.26° and 23.56° were assigned to the (200) reflection and (002)/(202) reflections of the α crystalline form of PA 6 [41]. The peak at 28.64° appears after polymer treatment in hot water and cannot be assigned for neither forms of the crystalline PA 6. When the polymer is exposed directly to water, water initiates degradation/hydrolysis reactions in the polymer.

Mixing H_2SeO_3 and Na_2SO_3 solutions leads to the release of Se according to the following reaction [42]:

$$Na_2SeO_{3(aq)} + 2Na_2SO_{3(aq)} + H_2SO_{4(aq)} \rightarrow Se_{(s)} + 3Na_2SO_{4(aq)} + H_2O_{(l)} \quad (11)$$

A red film was observed on PA 6 (Figure 3). The precipitate, characterised by XRD analysis (Figures 3 and 4), was identified as red amorphous selenium (a-Se).

Preprints (www.preprints.org) | NOT PEER-REVIEWED | Posted: 6 July 2023 doi:10.20944/preprints202307.0328.v1

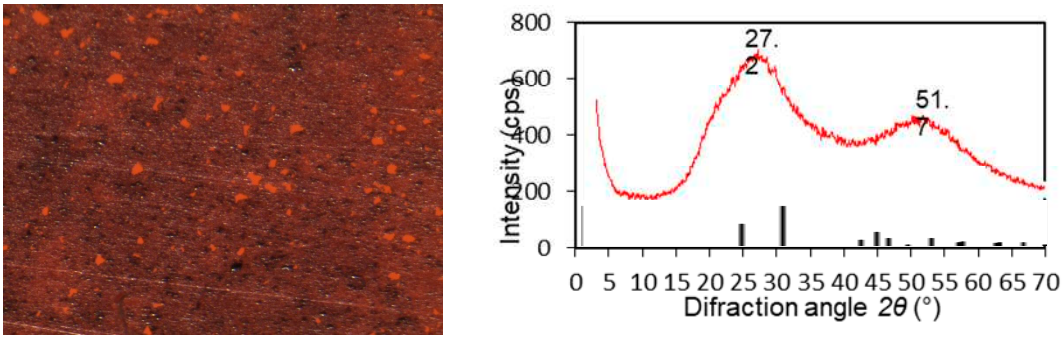

(**a**) (**b**)

Figure 3. (**a**) Optical micrograph of the red upper a-Se layer on a PA 6 membrane (×100 magnification); (**b**) XRD pattern of the a-Se upper layer scrub.

Because intensities of the diffraction peaks of PA 6 are very high and overlap with main peaks of the materials inserted/deposited on the polymer, the XRD patterns of the obtained composites were given in the 2θ assortment of 30–65°. As can be seen from Figure 4, in the a- Se/PA6 composite, Se formed at the end of reaction (9) is in the amorphous form, i.e., not detected by XRD analysis.

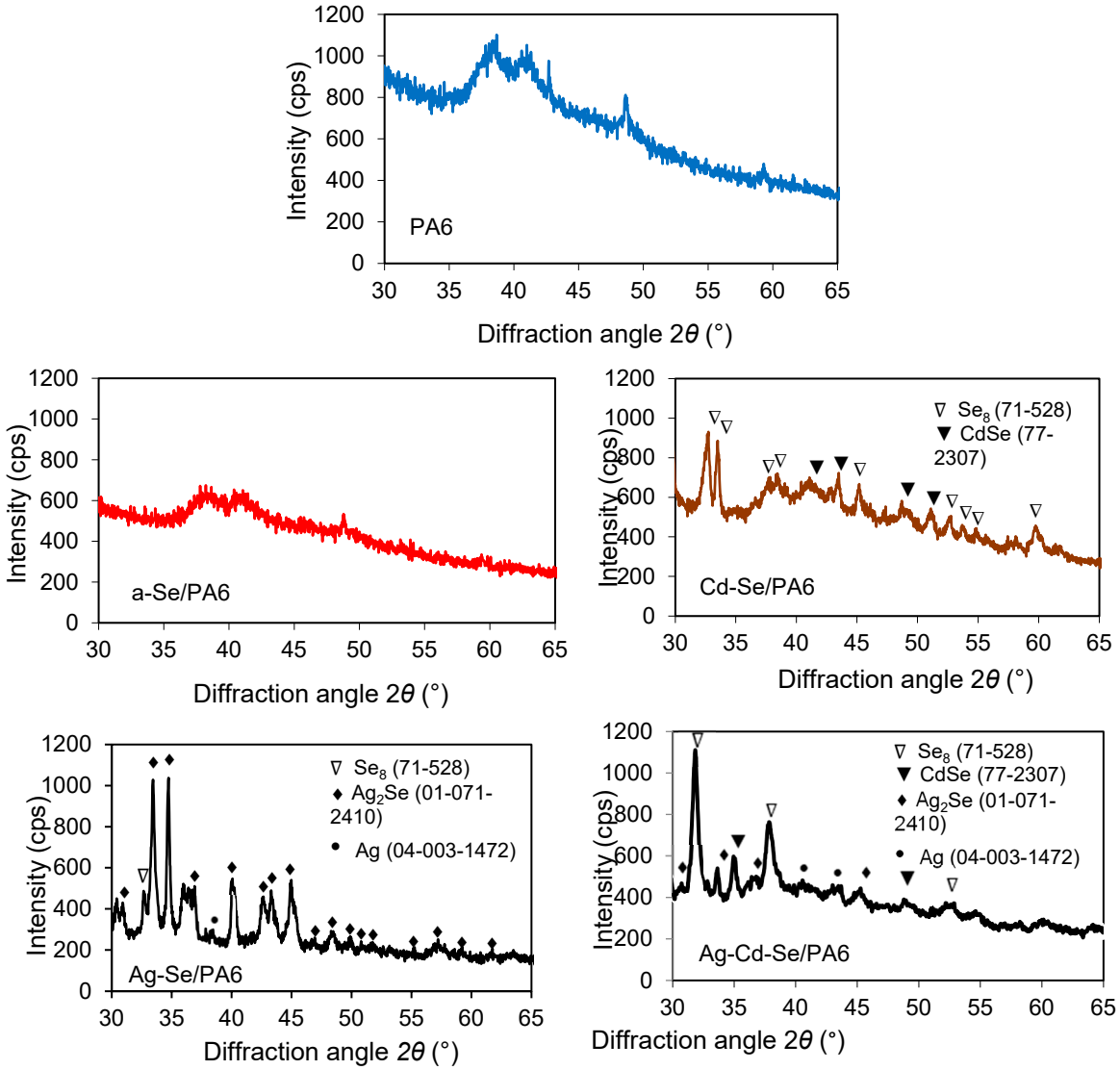

Figure 4. XRD diffractograms of boiled PA 6 and obtained composites. PA 6 peaks not shown.

The obtained positions of the diffraction peaks at 2θ 42.74°, 43.46°, 48.68°, 51.09° in the Cd-Se/PA6 composite (Figure 4) were compared with standard values and mainly indexed as CdSe (PDF 77-2307). The peaks at 2θ 32.66°, 33.49°, 37.64°, 38.46°, 45.16°, 52.66°, 53.77°, 54.83° and 59.73° are indexed as Se_8 (PDF no. 71-528) with hexagonal and monoclinic unit cells, respectively (Figure 4, Cd-Se/PA6 composite). It was found that CdSe has a polycrystalline nature with predominant (110) orientation plane. These experimental results agree well with the literature data. It is well known [43] that in the case of hexagonal lattices the strongest chemical bonds are formed by atoms located in a semi crystalline configuration on crystallographic planes (110) or (101).

Based on the analysis of the XRD results, it can be concluded that the immersion of the a-Se/PA6 nanocomposite in a $Cd(NO_3)_2$ solution at a temperature of 80±1 °C contributes to the gradual crystallisation of red a-Se into grey cr-Se. It is very reactive and reacts with many metal cations [44,45]. The solubility of a-Se ($2.2 \cdot 10^{-8}$ mol/dm^3 [46]) was approximately an order of magnitude higher than the solubility of cr-Se ($1.5 \cdot 10^{-9}$ mol/dm^3 [46]). The formation of CdSe can be explained by the following reaction [47–49]:

$$2Se_{(s)} + 3Cd^{2+}_{(aq)} + 3H_2O_{(l)} \rightarrow 2CdSe_{(s)} + CdSeO_{3(s)} + 6H^+_{(aq)}, \quad (12)$$

The formation of the Cd-Se/PA 6 composite leads to a colour change of from red to brown (Figure 1).

The Ag-Se-6/PA 6 nanocomposite shows diffraction peaks corresponding to the orthorhombic phase of Ag_2Se naumannite (PDF No. 01-071-2410). As can be seen from Figure 4, the dominant peak (121) of the orthorhombic system represents the preferred orientation along this plane. The identified peak positions are in good agreement with those indicated in the literature for Ag_2Se nanowires [50] and nanoparticles [51]. The diffraction pattern of the Ag-Se/PA 6 nanocomposite shows two sharp lines of approximately the same intensity along the (112) and (121) planes respectively. The reaction involved in this process can be summarised as the following [47–49]:

$$3Se_{(s)} + 6Ag^+_{(aq)} + 3H_2O_{(l)} \rightarrow 2Ag_2Se_{(s)} + Ag_2SeO_{3(s)} + 6H^+_{(aq)}, \quad (13)$$

The formation of Ag_2Se leads to a colour change from red to black. Together with the Ag_2Se phase, a minor amount of monoclinic Se_8 (PDF No. 71-528) at 2θ 32.66° Se_8 may remain unreacted in the deposited film phase. Ag-Se/PA6 composite (Figure 4) XRD analysis showed that not only Ag_2Se but also the metallic Ag phase (PDF No. 04-003-1472) was identified in the diffractogram. Typically, the metallic structure of Ag is depicted by a sharp XRD peak at 2θ 38.12° corresponding to the preferred (111) texture. Metallic Ag is the most likely impurity in chemically deposited Ag_2Se layers [50] as shown in the reaction as follows:

$$Se_{(s)} + 4AgNO_{3(aq)} + 3H_2O_{(l)} \rightarrow 4Ag_{(s)} + H_2SeO_{3(aq)} + 4HNO_{3(aq)}., \quad (14)$$

As discussed in [52], excess Ag can be introduced in several ways: in the form of adsorbed metal chains, in the form of point defects, or in the form of three-dimensional nano- or micro-inhomogeneities.

The XRD pattern of the Ag-Cd-Se/PA 6 composite shows the multiphase crystalline composition of the film. Compared to the XRD pattern of the Cd-Se/PA 6 composite, Se_8 and CdSe phases remain. The XRD peaks corresponding to CdSe are not shifted, which indicates the same structure, regardless of the cation exchange with Ag^+ ions and the appearance of new phases associated with orthorhombic Ag_2Se and metallic Ag. On Figure 4 also shows that the intensity of the peaks of the Ag-Cd-Se/PA 6 composite increases with the appearance of new phase, which additionally shows an increase in crystallinity. Broadening of the diffraction peaks is associated primarily with the finite sizes of the crystallites. The formation of Ag_2Se in Cd-Se/PA6 composite leads to a colour change from brown to black.

Since the other phases were not found in Cd-Se/PA6, Ag-Se/PA6 and Ag-Cd-Se/PA6 nanocomposites, it could be assumed that the SeO_3^{2-}, SO_3^{2-} and SO_4^{2-} ions diffused from the a-Se/PA 6, reacted with the Cd^{2+} and Ag^+ ions to form these compounds in solution near the sample area. In

Preprints (www.preprints.org) | NOT PEER-REVIEWED | Posted: 6 July 2023 doi:10.20944/preprints202307.0328.v1

another case, by-products of Equations (10) and (11) due to the sufficiently high solubility (Table 2, $CdSeO_3$ (K_{SP} = 5.0·10^{-9} (mol/dm^3)^2) and Ag_2SeO_3 (K_{SP} = 1.35·10^{-16} (mol/dm^3)^3) were removed from the surface of the samples by rinsing the as-synthesized composites with excess hot water.

The structural parameters of PA 6 and the prepared composites calculated from XRD data are listed in Table 1.

Table 1. Structural parameters of PA 6 and prepared composites calculated from XRD data.

Sample	Phase	2θ, °	D, nm	$\delta\times10^{15}$, line·m^{-2}	$\varepsilon\times10^{-3}$, line^{-2}·m^{-4}
PA6	PA6	23.5	16	3.70	2.11
a-Se/PA6	PA6	23.7	17	3.33	2.00
	a-Se	–	–	–	–
Cd-Se/PA6	PA6	23.5	17	3.38	2.01
	Se_8	33.5	33	0.89	1.04
	CdSe	42.7	40	0.63	0.87
Ag-Se/PA6	PA6	23.6	17	3.56	2.06
	Se_8	31.8	31	0.91	1.07
	Ag_2Se	33.8	34	0.85	0.98
	Ag	43.4	34	0.89	1.02
Ag-Cd-Se/PA6	PA6	23.7	17	3.58	2.08
	Se_8	31.8	30	1.10	1.15
	CdSe	48.7	37	0.74	0.94
	Ag_2Se	33.6	35	0.84	1.00
	Ag	43.5	34	0.88	1.03

A theoretical framework provides a general background to support our investigation. The sequence of phase formation in multicomponent systems depends on the structure of the starting material (SM). It is common knowledge that the exchange of cations can be achieved through simple mutual diffusion with other cations [53]. In addition, considering phase formation, the driving force of the solid-state interaction is also determined by the change in the Gibbs free energy, since the system always tends to the lowest possible free energy state [54]. The feasibilities of possible CE reactions were studied by thermodynamic deduction based on the thermodynamic law. CE reactions based on major difference in solubility product (K_{SP}) between the starting material (SM) and the final product (FP). Gibbs free energy (ΔG) for insoluble materials expressed according to Equation (15):

$$\Delta G = RT \times ln\frac{I_{CP}}{K_{SP}}, \quad (15)$$

where R—universal gas constant (8.319 J/mol·K), T—temperature (K), K_{SP}—the solubility product of the SM (in our case CdSe), I_{CP}—the product of the concentration of FP ions (in our case Ag_2Se). I_{CP} can be calculated according to Equation 16:

$$I_{CP} = C_{Ag^+}^2 \times C_{Se^{2-}}, \quad (16)$$

where C_{Ag^+} and $C_{Se^{2-}}$—the concentration of ions (mol/dm^3). In this way, the reaction of transition from a material with higher K_{SP} (CdSe) to a lower one (Ag_2Se) can proceed spontaneously. However, it is not easy to judge whether the CE reaction can proceed or not since this process is very complex and is associated with many factors: barrier to the activation energy of the phase transition, change in surface free energy, temperature, the active concentrations of ions in the solution, etc. [55]. Therefore, a more correct criterion should be the difference in solubility (S) of the SM and the FP (see Table 2).

Preprints (www.preprints.org) | NOT PEER-REVIEWED | Posted: 6 July 2023 doi:10.20944/preprints202307.0328.v1

Table 2. Standard Gibbs free energy (G) (298.15 K, 1 bar) [54], bond dissociation energies (BDE) [56], solubility product constants (K_{SP}) [38)] and calculated solubility (S) of CdSe and Ag_2Se phases.

Phase or ion	G, kJ/mol	BDE, kJ/mol	K_{SP}, $(mol/dm^3)^n$	S, mol/dm^3
a-Se	6.00± 2.2	–	–	$2.2\ 10^{-8}$
cr-Se	0.00	332.6 (Se–Se)	–	$1.5\ 10^{-9}$
Ag^+	77.11	–	–	–
Cd^{2+}	–77.16	–	–	–
CdSe	–141.60	127.6 ± 25.1	$1.0 \cdot 10^{-33}$	$3.16 \cdot 10^{-17}$
Ag_2Se	–46.90	210.0 ± 14.6	$3.1 \cdot 10^{-65}$	$3.14 \cdot 10^{-22}$

* n = 2 for CdSe, n = 3 for Ag_2Se.

The stoichiometric reactions at an interface between the Cd-Se/PA 6 and Ag^+ salt aqueous solution can be considered as follows:

$$CdSe_{(s)} + 2Ag^+_{(aq)} \rightarrow Ag_2Se_{(s)} + Cd^{2+}_{(aq)},\ \Delta G^\circ_{reac,298} = -144.60, \quad (17)$$

The negative values of $\Delta G^\circ_{reac,298}$ indicate that thermodynamic conditions are provided for the proceeding of this reaction. However, it should be emphasised that in the case of solid-phase interaction in multicomponent systems, phase formation at the precursor/solution interface is a dynamic non-equilibrium process that requires careful consideration of the mechanistic pathways along which they proceed [57]. Apparently, the determining criterion for the possibility of a thermodynamic reaction in hybrid materials is the solubility of CdSe in the starting Cd-Se/PA6 material. The higher solubility of CdSe (Table 2) favours the transformation into Ag_2Se. When Cd-Se/PA6 is immersed in $AgNO_3$ solution, Ag^+ reacts with Se^{2-} ions formed from the ionisation of dissolved CdSe leading to the formation of Ag_2Se particles, which results in the reduction of Cd^{2+} ions in the solution. Before explaining the formation of the Ag_2Se phase, it is necessary to discuss the active species that might be involved in the reaction path. Based on the discussion presented above, we speculated that the formation of Ag_2Se phases in the Cd-Se/PA6 composite could be explained through complex mechanism reactions: Ag^+ ions were attracted to the surfaces of metal chalcogenides particles due to the large specific area, then adsorbed Ag^+ replaced Cd^{2+} ions from the CdSe lattice and formed Ag_2Se. In parallel, some Ag^+ ions featuring relatively high ion diffusivity [58,59] propagate into the interior of the polymer and react with the cr-Se to form Ag_2Se according to reaction (13). The obtained composites (denoted in the text as a-Se/PA6, Cd-Se/PA6, Ag-Se/PA6 and Ag- Cd-Se/PA 6) were homogeneous with good adhesion.

3.2. AFM Analysis

The morphological changes of the PA 6 surface before and after subsequent chemical incorporation of a-Se, and Cd^{2+} and Ag^+ cations were characterized by AFM.

One can see that the surface morphology of all nanocomposites varies depending on the incorporated element. AFM was used to elucidate the formation mechanism and homogeneity of obtained composites. On a selected small scan area of 5 μm × 5 μm, 2D height data (Figure 5A) and 3D topographic (Figure 5B) AFM images of the respective PA 6 membrane, a-Se/PA 6, Cd-Se/PA 6, Ag-Se/PA 6 and Ag-Cd-Se/PA 6 nanocomposites with the corresponding measured topographic parameters are shown in Figure 5. The morphological pattern of PA 6 membrane revealed a wavy surface. a- Se/PA 6, Cd-Se/PA 6, Ag-Se/PA 6 and Ag-Cd-Se/PA 6 composites had a rough surface. The 3D topographic images (Figure 5B) show an irregular pattern resembling a valley of nodules. Since the composites did not have a pronounced texture but were characterized by a complex relief morphology, the roughness parameters were calculated from profilograms obtained for different surface areas (Figure 5C). The length of the scan areas was approximately 4.5–6.5 μm. Surface roughness is an important indicator of the quantitative characteristics of the sample surface. The average height, Z_{mean} (156.9 nm), and the average surface roughness, R_a (27.61 nm), of the a-Se/PA 6 composite are clearly different from those of the unreacted PA 6 membrane (Z_{mean} 60.4 nm, R_a 10.78 nm) (Figures 5A and 5B). As shown in Figure 5 local areas of the surface of the PA 6 membrane and the a-Se/PA 6 composite have different morphological structures. Simultaneously, isolated solid particles of amorphous Se (Figure 5) functioned

Preprints (www.preprints.org) | NOT PEER-REVIEWED | Posted: 6 July 2023 doi:10.20944/preprints202307.0328.v1

as seeds to start the formation of CdSe and Ag_2Se. When a-Se/PA 6 composite was exposed to an aqueous $Cd(NO_3)_2$ and $AgNO_3$ solutions, a-Se reacts with Cd^{2+} and Ag^+ cations to form insoluble CdSe and Ag_2Se nanoparticles that deposit in situ on the a-Se/PA 6 and produce the Cd-Se/PA 6 and Ag-Se/PA 6 composites (according to Equations (12) and (13)). The average height Z_{mean} (53.57 nm) and the average surface roughness R_a (9.82 nm) of the Cd-Se/PA 6 composite significantly decreased compared to the a-Se/PA 6 composite. It implies that CdSe formation proceeded mainly through deposited a-Se layers within the PA 6 surface. The average height Z_{mean} (35.10 nm) and the average surface roughness R_a (8.25 nm) of the Ag-Se/PA 6 composite significantly decreased compared to the a-Se/PA 6 composite. After exposure of the Cd-Se/PA 6 composite in an aqueous solution of $AgNO_3$, submicron pyramidal particles, presumably belonging to Ag_2Se (according to Equation 13), are found on the surface of the resulting Ag-Cd-Se/PA 6 composite (Figure 5). Pyramid-like structures with a lateral size of about 150 nm are also visible. Some of these particles aggregate on the composite surface. Small dark spots at the boundaries of grains and agglomerates may be due to depressions in the layers. From the roughness values presented in Figure 5, we can conclude that the quantitative parameters of the surface of the Ag-Se/PA 6 and Ag-Cd-Se/PA 6 composited decreased compared to the Cd-Se/PA 6 composite. For Ag-Cd-Se/PA 6 composite R_a decreased from 9.82 nm to 8.36 nm, and R_q decreased from 12.17 nm to 11.55 nm. In addition, the peak-to-valley roughness R_t of the surface of the Cd-Se/PA 6 and Ag-Cd-Se/PA 6 composites remain virtually unchanged. That confirmed our assumption about the formation of compact films. RMS is defined as the standard deviation of the surface height profile from the average height. The profilograms indicate a slightly asymmetric surface with more peaks than valleys (Figure 5C). It is important to note that the RMS of the deposited films decreased during the formation of CdSe, Ag_2Se and mixed CdSe-Ag_2Se nanoparticles compared to the a-Se films deposited on the PA 6 surface.

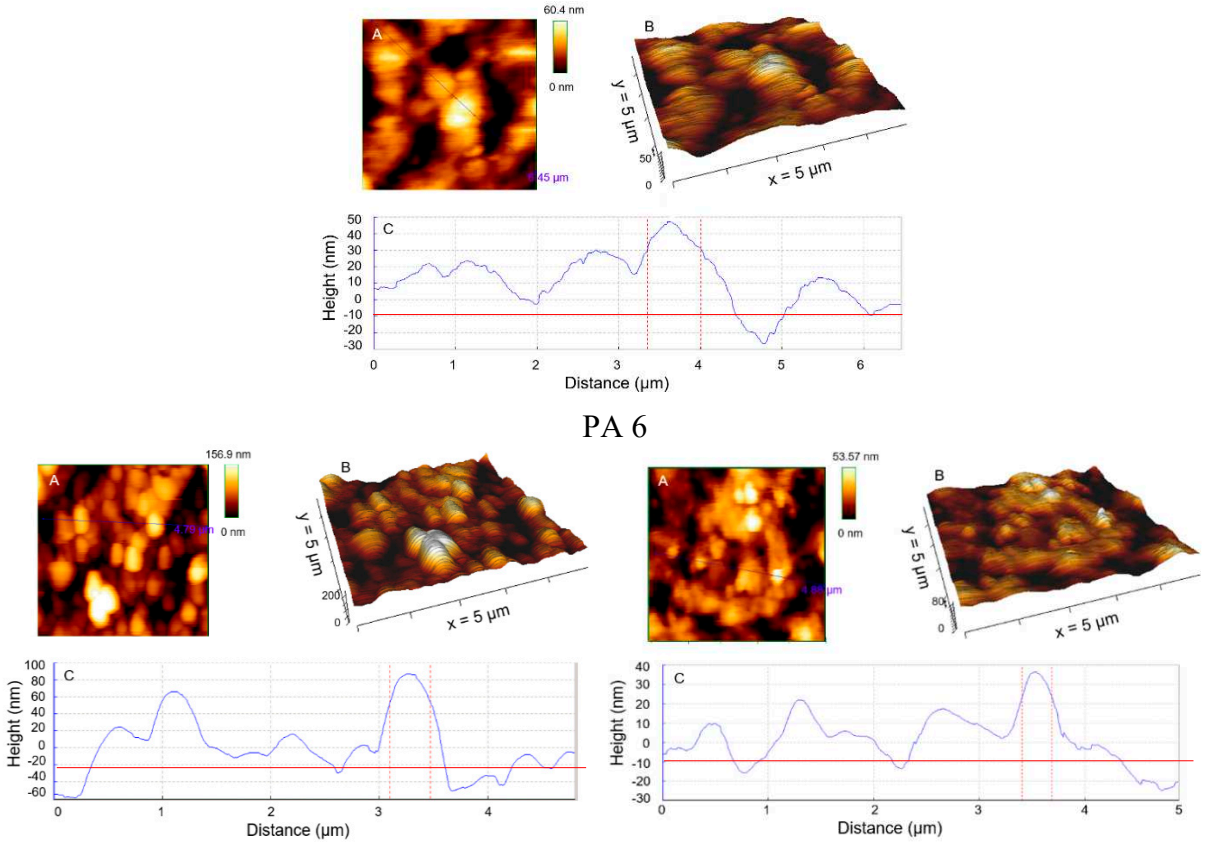

PA 6

a-Se/PA 6 Cd-Se/PA 6

Preprints (www.preprints.org) | NOT PEER-REVIEWED | Posted: 6 July 2023 doi:10.20944/preprints202307.0328.v1

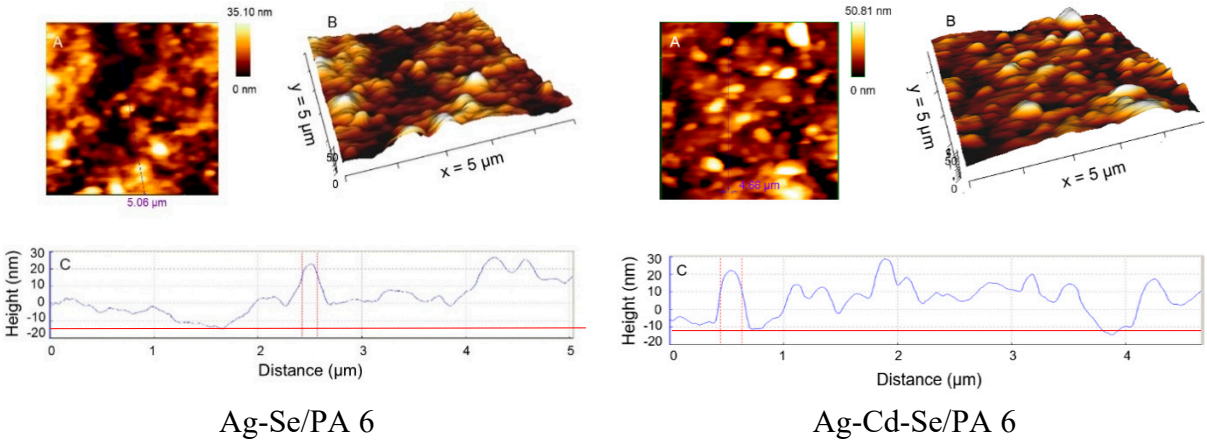

Figure 5. Sequential 2D height data (A), 3D AFM topographic images (B) and the height profile (of the blue line in A) (C) of PA 6 and the obtained nanocomposites.

3.3. ATR-FTIR Analysis

The FTIR study allows to discover the conformational structural changes of polymer chain as well as and the complexation and interaction between the polymeric matrices and inorganic nanoparticles. The ATR-FTIR spectra of the PA 6 and obtained nanocomposites within a wave number range from 650 to 1650 cm^{-1} are displayed in Figure 6. PA 6 consists of $(CH_2)_5$ segments separated by a parallel or antiparallel arrangement of secondary amide groups [60]. The bands related to NH–CO fragments are mainly affected by the mutual arrangement of H–bonds, while the vibrations from CH_2 groups reflect the effect of the chain conformation [61]. In PA 6 spectrum the absorption bands at 834 cm^{-1}, 929 cm^{-1}, 960 cm^{-1}, 1031 cm^{-1} and 1200 cm^{-1} (Table 3), confirm predominantly the α-crystalline phase. The spectral features at 1476 cm^{-1} and 1417 cm^{-1} represent CH_2 scissoring vibrations next to –NH and >C=O groups, respectively. The band at 1463 cm^{-1} corresponds to CH_2 scissoring vibrations. Two typical absorption bands at 1633 and 1535 cm^{-1} represents the amide I and II group, respectively.

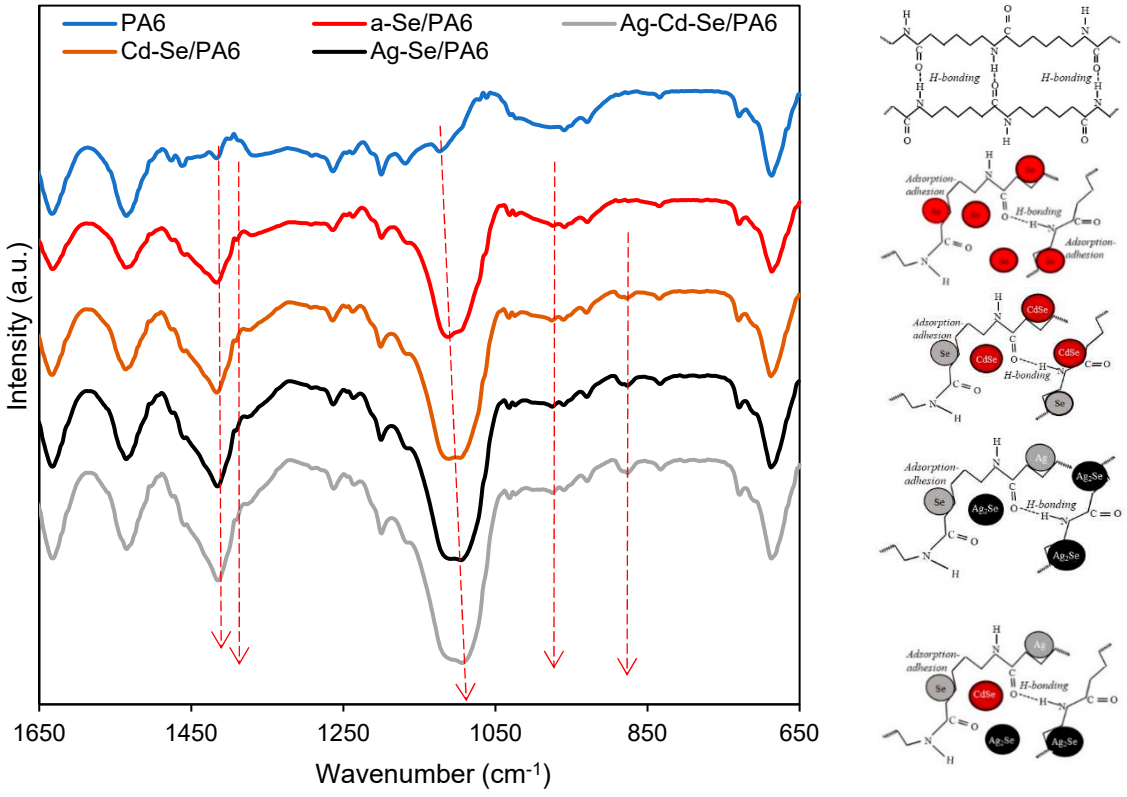

(**a**) (**b**)

 doi:10.20944/preprints202307.0328.v1

Figure 6. (**a**) FTIR spectra in the region of 1650–650 cm^{-1} of the PA 6 matrix and the obtained nanocomposites; (**b**) schematic diagram of the internal amide network in the PA 6 and possible network in the obtained composites.

Table 3. Band location and assignments of PA 6 and obtained nanocomposites spectra over wavenumber 1650–650 cm^{-1}.

Band location, cm^{-1}					Assignment
PA6	a-Se/PA6	Cd-Se/PA6	Ag-Se/PA6	Ag-Cd-Se/PA6	
687	687	687	687	687	C–C bending
730	730	729	730	729	CH_2 waging
834	835	833	833	833	CO–NH in plane
–	–	877	877	876	Cd-Se or/and Ag-Se
929	929	930	930	930	CO–NH in plane
960	959	961	960	960	CO–NH in plane (α crystalline)
–	974	976	975	975	CO–NH in plane (γ crystalline)
1023	1023	1025	1024	1024	trans C–C backbone conformation
1031	1031	1031	1032	1031	CO–NH in plane (α crystalline)
1124	1112	1112	1108	1094	C–C stretching (sym)
1169	1165	1166	1166	1165	N–C–O groups/CH_2 twisting
1200	1200	1200	1200	1201	C–CH bending (sym) CH_2 twisting
1238	1238	1236	1237	1235	
1264	1264	1261	1263	1263	C–N stretching (amide III)
1365	1371	1376	1377	1377	CH_2 twisting
–	1390	1392	1392	1391	C–C stretching (sym)
1417	1417	1417	1416	1415	CH_2 scissoring next to >C=O group
1463	1459	1460	1459	1459	CH_2 scissoring
1476	1475	1476	1475	1475	CH_2 scissoring next to N–H group
1535	1534	1536	1536	1535	C–N stretching and N–H bending of hydrogen-bonded N–H groups (amide II)
1633	1633	1633	1633	1632	C=O stretching (amide I)

The FTIR vibration bands of Se_8 rings are reported at 487.9 cm^{-1} and 737.7 cm^{-1} [62]. These peaks are absent in the FTIR spectrum of a-Se/PA 6, which confirms the XRD data that the inserted selenium is amorphous. Incorporation of solid inorganic nanoparticles into flexible polyamide network causes chain stretching. This should cause a conformational change in the chains of the polymer matrix [61,63]. It can be seen that most of the characteristic vibration bands of PA 6 in the wavenumber region from 650 to 1650 cm^{-1} *are retained* in the FTIR spectrum of a-Se/PA 6; however *the intensity of the peaks changes*: some of them become more intense and some *of them expand*. *It can be concluded* that as a-Se nanoparticles are introduced between the polymer chains and stretched, the position and intensity of the peaks change. Thus, the peak of neat PA 6 at 1124 cm^{-1} in a-Se/PA 6 spectrum shifts to 1112 cm^{-1}, and two new small peaks are recorded at 974 cm^{-1} and 1390 cm^{-1}. The shoulder at 974 cm^{-1} shows the appearance of a small amount of the γ crystalline form of PA 6, and C–C symmetry vibration causes IR absorption at the *1390 cm^{-1} [64]*.

CdSe and Ag_2Se have no specific vibrations in the spectral region between 650 and 1650 cm^{-1}, but exhibit absorption in the region of 200–400 cm^{-1} [65–67]. Thus, it is possible to avoid the problem of overlapping of metal selenides and PA 6 characteristic peaks. The IR spectra of the Cd-Se/PA 6, Ag-Se/PA 6 and Ag-Cd-Se/PA 6 composites are very similar to the a-Se/PA 6 spectrum, but show an even greater shift of the peak at 1112 cm^{-1} to lower frequencies (Table 3) and the appearance of another new peak at 877 cm^{-1}. By analogy with data reported for CdSe [61], those weak vibrations can be attributed to the Cd–Se or Ag–Se bond. Another dimension of the

Preprints (www.preprints.org) | NOT PEER-REVIEWED | Posted: 6 July 2023 doi:10.20944/preprints202307.0328.v1

functionality and complexity of inorganic-organic materials is introduced if the selenides are combined with each other. For example, the negative energies of chemical band formation of CdSe and Ag_2Se promote the creation of Ag–Cd–Se– interfacial bonds, which leads to non-selective nucleation in Ag_2Se/CdSe hetero-nanostructures [68]. Thus, the peak at 1108 cm^{-1} in the IR spectrum of the Ag-Se/PA 6 composite shifts to 1094 cm^{-1} in the IR spectrum of the Ag-Cd-Se/PA 6 composite.

The shift and broadening of the C–C stretching vibration peaks, accompanied by the appearance of new small peaks of low intensity, allows us to conclude that we are observing the formation of intermediate structures inside the polyamide chains. Thus, we can be conclude, that the spectral changes after insertion of a-Se and ions of Cd^{2+} and Ag^{+} ions with respect to PA 6 sample belong to the bands related to the C–C conformation of the main chain. The peak at 1124 cm^{-1}, arising from the all-trans C–C conformation of the main chain, loses its spectral position. In addition, the peak is broadened, and its intensity noticeably increases in all spectra of the obtained composites (Figure 6).

3.4. UV-Vis Analysis

The experimental absorption spectra are presented in Figure 7.

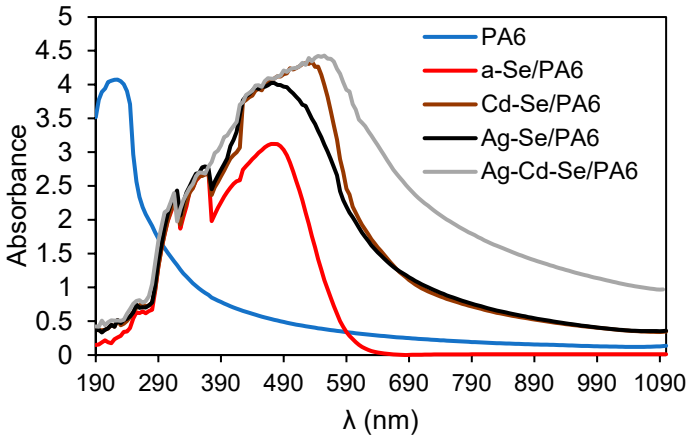

Figure 7. Absorption spectra of PA 6 and obtained composites.

The absorption spectrum of PA6, (Figure 7.) displays absorption peak at 225 nm. The color of the obtained a-Se/PA6 nanocomposite becomes red, suggesting the change of optical properties. In the UV-Vis absorption spectrum of the a-Se/PA6 nanocomposite, a number of peaks appear at 320 nm, 370 nm, and 475 nm, which characterize the formation of a band structure: red a-Se nanoparticles are introduced into the system of PA 6 micropores at the first stage, and then they combine into aggregates and agglomerates. According to the literature data [69,70] bulk a-Se absorbs 475 nm light.

In the UV-Vis spectrum of the Cd-Se/PA6 nanocomposite, peaks appear at the same 320 nm and 370 nm, which are related to Se nanoparticles and agglomerates, and a new peak at 535 nm. According to the literature data, CdSe quantum dots have a wide absorption band in the spectral range of 410–545 nm [71], and the absorption maximum of CdSe nanocrystals, depending on the particle size, is in the range from 492 to 578 nm [72]. Therefore, the peak at 535 nm can be attributed to CdSe.

In Ag-Se/PA6 UV-Vis spectrum the peaks appear at 320 nm, 365 nm and 475 nm. Ag_2Se nanoparticles absorb in a wide spectral region from 300 to 600 nm [73], while two sharp peaks are observed in the spectrum of quantum dots at 440 and 607 nm, respectively [74]. Monodisperse silver nanoparticles, depending on the size, shape, and distribution in nanostructures, have two absorption bands; one broad peak in the range 420-430 nm and a shoulder at 580-590 nm [75]. Therefore, a broad peak from 380 to 590 nm with a maximum at 475 nm can be attributed to the Ag_2Se phase with a small amount of Ag nanoparticles.

Preprints (www.preprints.org) | NOT PEER-REVIEWED | Posted: 6 July 2023 doi:10.20944/preprints202307.0328.v1

In Ag-Cd-Se/PA6 nanocomposite UV-Vis spectrum the peaks appear at 315 nm and 555 nm. According to the literature data [76–78], the introduction of Ag^+ ions into CdSe nanocrystals via the CE reaction does not lead to noticeable changes in the absorption spectra of CdSe in the UV-visible region. In contrast, other authors suggested that the formation of the CdSe-Ag_2Se core-shell leads to the complete disappearance of the CdSe absorption peak in the UV-Vis spectra [79]. Thus, it can be stated that the absorption spectrum of the Ag-Cd-Se/PA6 composite is a superposition of the individual absorption spectra of the CdSe, Ag_2Se, and Ag phases, its absorption edge is shifted to the longer wavelength region, and their absorption increases in the range of 315–555 nm compared to with the region (320–535 nm) of Cd-Se/PA6 and Ag-Se/PA6 composites. This red shift of the λ_g may be related to the common complex alignment of the valence and conduction bands, as well as to the presence of multiple defects and vacancies. The determination of the phase composition of the obtained composites according to the data of optical studies is in good agreement with the XRD data.

The experimental UV-Vis spectra better correspond to the rectilinear section on the graphs $A^2 \cdot \lambda^{-2} = f(\lambda^{-1})$ (Figure 8), which confirms the direct transitions of the obtained nanocomposites.

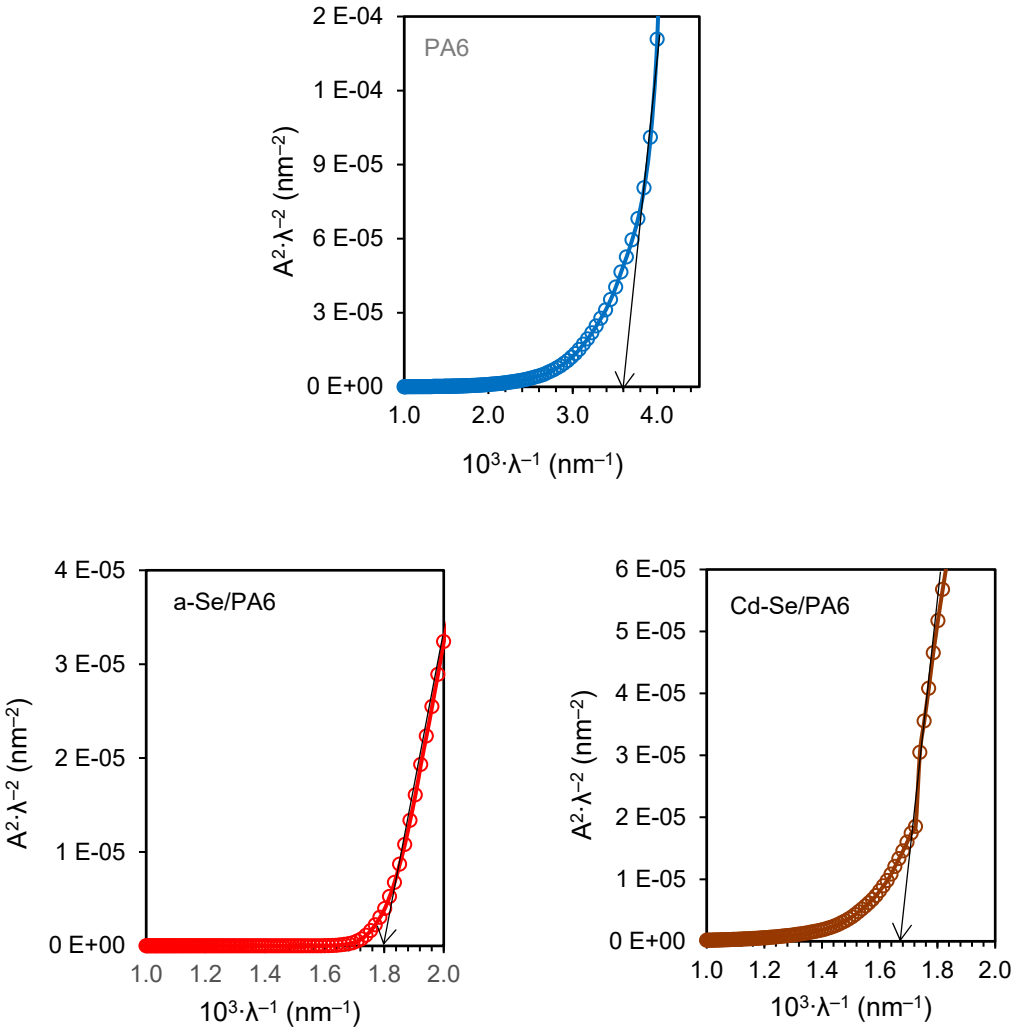

Preprints (www.preprints.org) | NOT PEER-REVIEWED | Posted: 6 July 2023 doi:10.20944/preprints202307.0328.v1

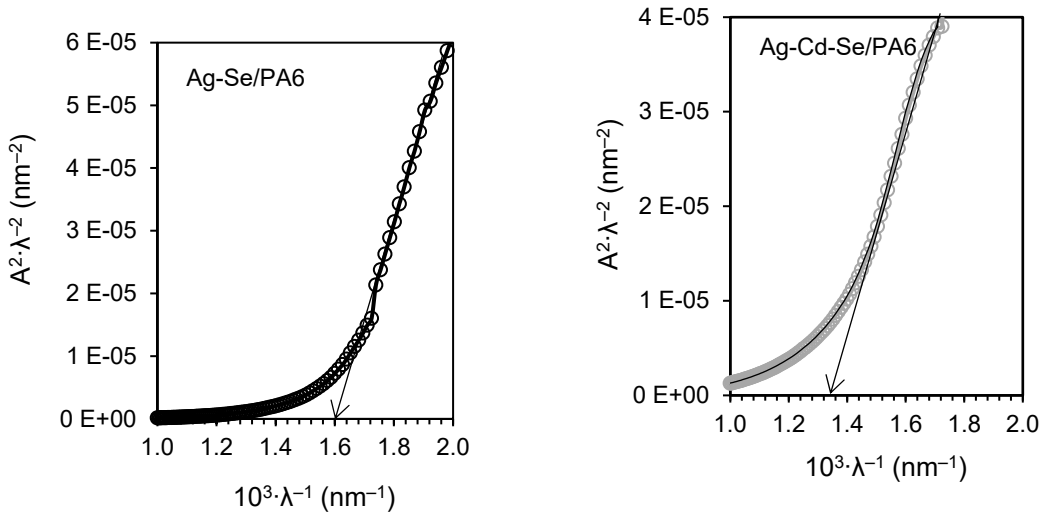

Figure 8. Dependence $A^2 \cdot \lambda^{-2}$ on λ^{-1} for the PA 6 membrane and obtained nanocomposites.

All the calculated optical parameters are given in Table 4 for comparison.

Table 4. The optical parameters of PA6 and studied nanocomposites.

Composite	λ_g, nm	E_g, eV	Eu, eV	σ	$E_{e\text{-}p}$, eV	χ
PA 6	278	4.46± 0.02	1.31	0.020	33.33	11.99
a-Se/PA 6	556	2.23± 0.02	0.95	0.027	24.69	5.99
Cd-Se/PA 6	605	2.05± 0.02	0.39	0.066	10.10	5.51
Ag-Se/PA 6	625	1.98± 0.02	0.55	0.047	14.18	5.32
Ag-Cd-Se/PA 6	756	1.64± 0.02	0.69	0.037	18.02	4.41

The decrease in E_g of each subsequent nanocomposite compared to PA 6 is due to a change in the they optical properties. E_g of nanocomposites can be affected many factors, such as composition, particle size and distribution, shape, agglomeration/aggregation state, solubility, surface morphology/topography, structure crystallinity, and many different structural defects or deformations [80,81]. The wavelength at which the signal gets saturated is interpreted as being the value of the absorption edge or the E_g of the semiconductor. For a-Se/PA6 composite E_g is 2.23± 0.02 eV. E_g measured for bulk a-Se is 1.99 ± 0.02 eV [82]. Introduction of Cd^{2+} ions proseed at 80 °C, and at heat treatment amorphous Se crystallizes. E_g measured for cr-Se is 1.85 ± 0.02 eV [82]. An increase in the crystallinity of the obtained composites (Figure 4) and the carrier concentration is accompanied by a decrease in E_g from 2.05±0.02 eV for the Cd-Se/PA 6 composite to 1.64±0.02 eV for the Ag-Cd-Se/PA 6 composite (Table 4). The obtained values are in good agreement with the literature data: CdSe and Ag_2Se have a band gap of 1.9 eV [20] and 1.8 eV [21], respectively.

One of the sources of unfavorable recombination is the subband absorption tail, which is characterized by the Urbach energy. Absorption tails are defined as densities of states that extend from the bands into the band gap of the photoactive layer. Tail states inside the band gap act as traps and recombination centers and trap a charge carrier. The Eu is influenced by thermal and structural disturbances in semiconductor materials [83–85]. In this work, we analyze structure-dependent Eu. The Urbach energy plots were constructed and shown in Figure 9, and the calculated values are given in Table 4. Eu reflects the density of states in the band tails and, hence, the local microstructural disorder [86]. As can be seen from the values presented in Table 4, the Eu of PA 6 is 1.31 eV, which is higher as compared with obtained nanocomposites. The relatively high value of Eu indicates a greater propensity for the transformation of weak structural bonds into defects [87]. The a-Se/PA 6 nanocomposite (amorphous phase) is more structurally disordered. With the

Preprints (www.preprints.org) | NOT PEER-REVIEWED | Posted: 6 July 2023 doi:10.20944/preprints202307.0328.v1

stepwise incorporation of Cd^{2+} and Ag^{+} ions, *Eu* decreases. This may be due to an increase in the structural ordering of nanocomposites, which is confirmed by an increase in crystallinity detected by XRD analysis. In addition, it was previously reported [88] that thicker selenide films have less structural randomness, since with an increase in the thickness and density of the layers, structural defects are minimized, which minimizes the *Eu*. The formation of compact these films was confirmed by AFM analysis.

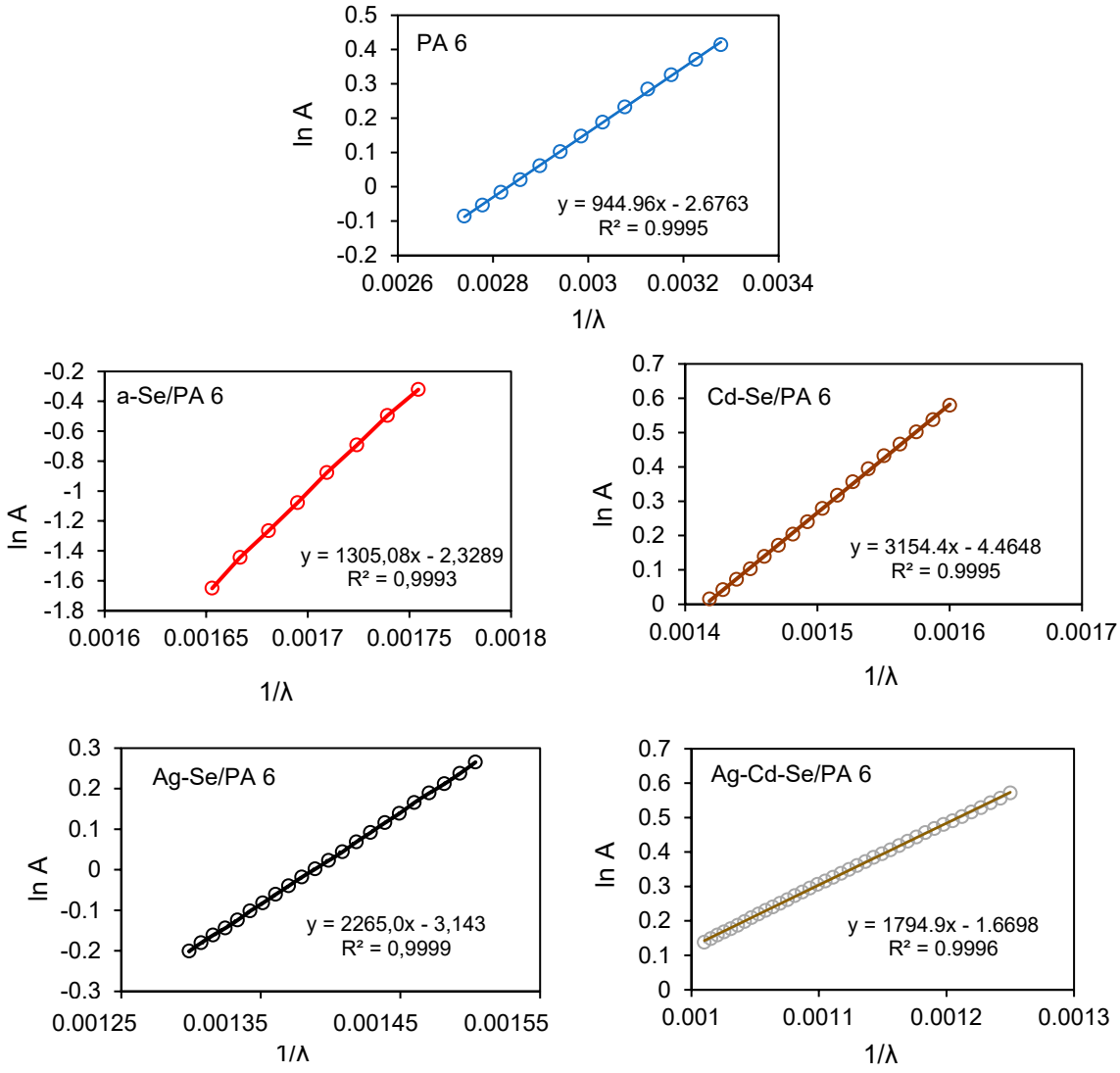

Figure 9. Urbach plots for PA6 membrane and obtained nanocomposites.

The σ characterizes the broadening of the optical absorption edge arising from the electron-phonon interactions [40,89]. The steepness parameter of PA 6 is lower than that of the obtained nanocomposites at the same temperature (Table 4). The lower differences in electronegativity decrease the orbital overlap, and decrease the band gap.

4. Conclusions

To sum up, the amorphous Se films conjugated with PA 6 were successfully obtained by exposing the PA 6 membrane to an acidified aqueous solution of H_2SeO_3 and Na_2SO_3. The surface morphology of the a-Se/PA6 consists of granular amorphous Se nanoparticles. This texture ensures optimal deposition of the next phase. The use of prepared a-Se/PA 6 composites opens the way for the stepwise incorporation of Cd^{2+} and Ag^{+} ions by a chemical methods. The positions of the

diffraction peaks in the Cd-Se/PA 6 composite were mainly indexed as hexagonal CdSe and monoclinic Se_8. XRD clearly shows that the Cd-Se/PA 6 and Ag-Se/PA 6 films are polycrystalline and exhibit a phase transformation from a-Se to a Se_8 monoclinic structure. The XRD pattern of the Ag-Cd-Se/PA 6 composite obtained by the CE method showed a complex crystalline composition of the film with peaks of monoclinic Se_8, hexagonal CdSe, orthorhombic Ag_2Se and metallic Ag. The obtained composites have an inhomogeneous surface morphology in the form of nanosized particles. ATR-FTIR spectroscopy revealed the interaction between PA 6 and inorganic components, which causes obvious conformational changes in PA 6 chains. The resulting composites differ in color, which affects and their optical properties. The optical spectra show that the nanostructured films have a high absorption coefficient in the visible region. The studied composites are direct band gap semiconductors, which exhibit a redshift of the band gap from 2.23 eV for the a-Se/PA 6 to 1.64 eV for the Ag-Cd-Se/PA 6 composite due to a change in chemical composition and can be promising in science for implantable microdevices, as well as for solar electronics. E_U and σ studies describe the broadening of solar absorption edges around optical band gaps, which correlates with the polycrystalline composition and heterogeneous surface morphology.

Author Contributions: Conceptualization, V.K.; methodology, V.K.; software, V.K.; validation, E.S.. and V.K.; formal analysis, E.S.; investigation, E.S.; resources, V.K.; data curation, V.K.; writing—original draft preparation, E.S.; writing—review and editing, V.K.; visualization, E.S.; supervision, V.K.; funding acquisition, V.K. All authors have read and agreed to the published version of the manuscript.

Funding: This research was funded by the Doctoral Fund of Kaunas University of Technology No. A-410, approved 26th of June, 2019.

Data Availability Statement: Data is contained within the article.

Conflicts of Interest: The authors declare no conflict of interest.

References

1. Park, Y.; Advincula, R.C. Hybrid semiconductor nanoparticles: π-conjugated ligands and nanostructured films. *Chem. Mater.* **2011**, *23*, 4273–4294. http://dx.doi.org/10.1021/cm201199u.
2. Liu, R. Hybrid organic/inorganic nanocomposites for photovoltaic cells. *Materials* **2014**, *7*, 2747–2771. http://dx.doi.org/10.3390/ma7042747.
3. Soler-Illia, G.J.; Azzaroni, O. Multifunctional hybrids by combining ordered mesoporous materials and macromolecular building blocks. *Chem. Soc. Rev.* **2011**, *40*, 1107–1150. http://dx.doi.org/10.1039/C0CS00208A.
4. Willner, I.; Willner, B. Functional nanoparticle architectures for sensoric, optoelectronic, and bioelectronic applications. *Pure Appl. Chem*. **2002**, *74*, 1773–1783. http://dx.doi.org/10.1351/pac200274091773.
5. Di Luccio, T.; Piscopiello, E.; Laera, A.M.; Antisari, M.V. Structural studies of thin films of semiconducting nanoparticles in polymer matrices. *Mater. Sci. Eng. C* **2007,** *27*, 1372–1376. https://doi.org/10.48550/arXiv.cond-mat/0607488.
6. Gates, B.; Mayers, B.; Cattle, B.; Xia, Y. Synthesis and characterization of uniform nanowires of trigonal selenium. *Adv. Funct. Mater*. **2002,** *12(3)*, 219–227. https://doi.org/10.1002/1616-3028(200203)12.
7. Jiang, F.; Cai, W.; Tan, G. Facile Synthesis and optical properties of small selenium nanocrystals and nanorods, *Nanoscale Res. Lett.* **2017,** *12*, 401. http://dx.doi.org/10.1186/s11671-017-2165-y.
8. *Guha, S.*; Munekata, H.; LeGoues, F.K.; Chang, L.L. Growth mode and dislocation distribution in the ZnSe/GaAs (100) system. *Appl. Phys. Lett*. **1992,** *60*, 3220. https://doi.org/10.1063/1.107465.
9. Bhatnagar, A.K.; Venugopal Reddy, K.; Srivastava, V. Optical energy gap of amorphous selenium: effect of annealing. J. Phys. D: Appl. Phys. **1985,** *18*, 149–l53. http://iopscience.iop.org/0022-3727/18/9/001.
10. Thayer, J.S. A Review of: Selenium. In *Synthesis and Reactivity in Inorganic and Metal-Organic Chemistry*, Zingaro, R.A., Cooper, W.C. Eds.; Van Nostrand Reinhold, New York, 1974, xvii, 5(2) 159–160. https://doi.org/10.1080/00945717508057312.
11. Afzaal, M.; O'Brien, P. Recent developments in II–VI and III–VI semiconductors and their applications in solar cells. *J. Mater. Chem*. **2006,** *16*, 1597–1602. http://dx.doi.org/10.1039/B512182E.
12. Gao, Q.; Wang, W.; Lu, Y.; Cai, K.; Li, Y.; Wang, Z.; Wu, M.; Huang, C.; He, J. High power factor Ag/Ag_2Se composite films for flexible thermoelectric generators. *ACS Appl. Mater. Interface* **2021,** *13(12)*, 14327–14333. https://doi.org/10.1021/acsami.1c02194.
13. Wu, M.; Cai, K.; Li, X.; Li, Y.; Liu, Y.; Lu, Y.; Wang, Z.; Zhao, W.; Wei, P. Ultraflexible and high-thermoelectric-performance sulfur-doped Ag_2Se film on nylon for power generators. *ACS Appl. Mater. Interfaces* **2022**, *14(3)*, 4307–4315. https://doi.org/10.1021/acsami.1c21701.

14. Roy, S.; Tuinenga, C.; Fungura, F.; Dagtepe, P.; Chikan, V.; Jasinski, J. Progress toward producing n-type CdSe quantum dots: tin and indium doped CdSe quantum dots. *J. Phys. Chem. C*, **2009**, *113(30)*, 130008–13015. https://doi.org/10.1021/jp8113946.
15. Liu, J.; Zhao, Q.; Liu, J.L.; Wu, Y.S.; Cheng, Y.; Ji, M.W.; Qian, M.H.; Hao, W.C.; Zhang, L.J.; Wei, X.J.; Wang, S.G.; Zhang, J.T.; Du, Y.; Dou S.X.; Zhu, H.S. Heterovalent-doping-enabled efficient dopant luminescence and controllable electronic impurity via a new strategy of preparing II–VI nanocrystals. *Adv. Mater.* **2015**, *27*, 2753–2761. https://doi.org/10.1002/adma.201500247.
16. Wang, F.D.; Dong, A.G.; Buhro, W.E. Solution–liquid–solid synthesis, properties, and applications of one-dimensional colloidal semiconductor nanorods and nanowires. *Chem. Rev.*, **2016**, *116(18)*, 10888–10933. https://doi.org/10.1021/acs.chemrev.5b00701.
17. Coughlan, C.; Ibanez, M.; Dobrozhan, O.; Singh, A.; Cabot, A.; Ryan, K.M. Compound copper chalcogenide nanocrystals. *Chem. Rev.* **2017**, *117*, 5865–6109. https://doi.org/10.1021/acs.chemrev.6b00376.
18. Liu, J.; Zhang, J. Nanointerface chemistry: lattice-mismatch-directed synthesis and application of hybrid nanocrystals. *Chem. Rev.* **2020**, *120*, 2123–2170. https://doi.org/10.1021/acs.chemrev.9b00443.
19. Agranovich, V.M.; Gartstein, Y.N.; Litinskaya, M. Hybrid resonant organic–inorganic nanostructures for optoelectronic applications. *Chem. Rev.* **2011**, *111*, 5179–5214. http://dx.doi.org/10.1021/cr100156x.
20. Mehta, C.; Abbas, J.M.; Saini, G.S.S.; Tripathi, S.K. Effect of deposition parameters on the optical and electrical properties of nanocrystalline CdSe. *Chalcogenide Letters* **2007**, *4(11)*, 133–138.
21. Pejova, B.; Najdoski, M.; Grozdanov, I.; Dey, S.K. Chemical bath deposition of nanocrystalline (111) textured Ag_2Se thin films. *Mater. Lett.* **2000**, *43*, 269–273. https://doi.org/10.1016/S0167-577X(99)00272-4.
22. Gates, B.; Yin, Y.; Xia, Y. A Solution-phase approach to the synthesis of uniform nanowires of crystalline selenium with lateral dimensions in the range of 10-30 nm. *J. Am. Chem. Soc.* **2000**, *122*, 12582–12583. https://doi.org/10.1021/ja002608d.
23. Murty, A.S.R. Thiourea in analysis. I. Estimation of selenium and tellurium. *Indian J. Chem.* **1965**, *3(7)*, 298–299.
24. Li, Z.; Huang, D.; McDonald, L.M. Heterogeneous selenite reduction by zero valent iron steel wool. *Water Sci. Technol.* **2017**, *75(4)*, 908–915. https://doi.org/10.2166/wst.2016.574.
25. Liang, L.; Yang, W.; Guan, X.; Li, J.; Xu, Z.; Wu, J.; Huang, Y.; Zhang, X. Kinetics and mechanisms of pH-dependent selenite removal by zero valent iron. *Water Res.* **2013**, *47*, 5846–5855. https://doi.org/10.1016/j.watres.2013.07.011.
26. Liang, L.P.; Jiang, X.; Yang, W.J.; Huang, Y.Y.; Guan, X.H.; Li, L.N. Kinetics of selenite reduction by zero-valent iron. *Desalin. Water Treat.* **2015**, *53*, 2540–2548. https://doi.org/10.1080/19443994.2013.862868.
27. Jain, R.; Jordan, N.; Schild, D.; van Hullebusch, E.D.; Weiss, S.; Franzen, C.; Farges, F.; Hübner, R.; Lens, P.N.L. Adsorption of zinc by biogenic elemental selenium nanoparticles. *Chem. Eng. J.* **2015**, *260*, 855-863. https://doi.org/10.1016/j.cej.2014.09.057.
28. Misra, G.J.; Tandon, J.P. Gravimetric determination of selenium using copper chloride as reducing agent. *Indian J. Chem.* **1967**, *5(11)*, 560–562.
29. Kalaparthi, R.; Korapu, S.; Gandam, H.; Kurimella, V.R. Synthesis of selenium nanoparticles using sodium selenite [Se(IV)] as a precursor and titanium(III) chloride as a reducing agent. *Int. J. Eng. Res.* **2020**, *9(4)*, 359–363. http://dx.doi.org/10.17577/IJERTV9IS040384.
30. Geoffroy, N; Demopoulos, G.P. Stannous chloride—an effective reducing agent for the removal of selenium(IV) from acidic solution. *J. Chem. Technol. Biotechnol.* **2012**, *87*, 983–989. http://dx.doi.org/10.1002/jctb.3708.
31. Geoffroy, N; Demopoulos, G.P. Reductive precipitation of elemental selenium from selenious acidic solutions using sodium dithionite. *Ind. Eng. Chem. Res.* **2009**, *48*, 10240–10246. http://dx.doi.org/10.1021/ie9008502.
32. Vieira, A.P.; Stein, E.M.; Andreguetti, D.X.; Cebrián-Torrejón, G.; Doménech-Carbó, A.; Colepicolod, P.; Ferreira, A.M.D.C. "Sweet Chemistry": a green way for obtaining selenium nanoparticles active against cancer cells. *J. Braz. Chem. Soc.* **2017**, *28(10)*, 2021–2027. http://doi.org/10.21577/0103-5053.20170025.
33. Vahdati, M.; Moghadam, T.T. Synthesis and characterization of selenium nanoparticles lysozyme nanohybrid system with synergistic antibacterial properties. *Sci. Rep.* **2020**, *10(1)*, 510. https://doi.org/10.1038/s41598-019-57333-7.
34. Hoffmann, J.E. Recovering selenium and tellurium from copper refinery slimes. *JOM* **1989**, *41(7)*, 33–37. https://doi.org/10.1007/BF03220269.
35. Kunita, M.H.; Girotto, E.M.; Radovanovic, E.; Gonçalves, M.C.; Ferreira, O.P.; Muniz, E.C.; Rubira, A.F. Deposition of copper sulfide on modified low-density polyethylene surface: morphology and electrical characterization. *Appl. Surf. Sci.* **2002**, *202(3–4)*, 223–231. https://doi.org/10.1016/S0169-4332(02)00938-8.
36. Essaidia, H.; Gantassi, A.; Touihria, S.; Ouerfelli, J. Tuning the structural, optical and electrical properties of $AgInSe_2$ thin films prepared by sequentially deposited silver and indium nano-films under vacuum. *Optik* **2019**, *182*, 866–875. https://doi.org/10.1016/j.ijleo.2018.11.170.

37. Nguyen, H.Q. Synthesis and optical properties of CdSe nanocrystals and CdSe/ZnS core/shell nanostructures in non-coordinating solvents. *Adv. Nat. Sci: Nanosci. Nanotechnol.* **2010**, *1*, 25004. https://doi.org/10.1088/2043-6254/1/2/025004.
38. Souri, D.; Tahan, Z.E. A new method for the determination of optical band gap and the nature of optical transitions in semiconductors. *Appl. Phys. B: Lasers Opt.* **2015**, *119*, 273–279. https://doi.org/10.1007/s00340-015-6053-9.
39. Souri, D.; Shomalian, K. Band gap determination by absorption spectrum fitting method (ASF) and structural properties of different compositions of (60−x) V_2O_5–40TeO_2–xSb_2O_3 glasses. *J. Non Cryst. Solids* **2009**, *355*, 1597–1601. https://doi.org/10.1016/j.jnoncrysol.2009.06.003.
40. Solaymani, S.; Talu, S.; Nezafat, N.B.; Dejam, L.; Shafiekhani, A.; Ghaderi, A.; Zelati, A. Optical properties and surface dynamics analyses of homojunction and hetrojunction Q/ITO/ZnO/NZO and Q/ITO/ZnO/NiO thin films. *Results Phys.* **2021**, *29*, 104679. https://doi.org/10.1016/j.rinp.2021.104679.
41. Xu, S.; Ye, L. Synthesis and properties of monomer cast nylon-6-*b*-polyether amine copolymers with different structures, R. Soc. Chem. Adv. **2015**, 5, 32460–32468. http://dx.doi.org/10.1039/c5ra03589a.
42. 16—Selenium, Tellurium and Polonium, In *Chemistry of the Elements*, 2nd ed.; Greenwood, N.N.; Earnshaw, A. Eds.; Elsevier Ltd., Butterworth-Heinemann, 1997; Volume 16, pp. 747–788. https://doi.org/10.1016/B978-0-7506-3365-9.50022-5.
43. Mahieu, S.; Ghekiere, P.; Depla, D.; de Gryse, R. Biaxial alignment in sputter deposited thin films. *Thin Solid Films* **2006**, *515(4)*, 1229–1249. https://doi.org/10.1016/j.tsf.2006.06.027.
44. Park, S.H.; Choi, J.Y.; Lee, Y.H.; Park, J.T.; Song, H. Formation of metal selenide and metal-selenium nanoparticles using distinct reactivity between selenium and noble metals. *Chem Asian J.* **2015**, *10(7)*, 1452–6. http://dx.doi.org/10.1002/asia.201500191.
45. Yanhui, Z.; Xu, M.; Liu, Y.; Bai, Y.; Deng, Y.; Liu, J.; Chen, L. Green synthesis of Se/Ru alloy nanoparticles using gallic acid and evaluation of their anti-invasive effects in HeLa cells. *Colloids Surf. B* **2016**, *44*, 118–124. http://dx.doi.org/10.1016/j.colsurfb.2016.04.004.
46. Olin, Å.; Noläng, B.; Osadchii, E.G.; Öhman, L.-O.; Rosén, E. *Chemical Thermodynamics of Selenium*, 1st ed.; Elsevier Science, 2005. 894 p. https://www.oecd-nea.org/dbtdb/pubs/vol7-selenium.pdf.
47. Ozin, G.A.; Arsenault, A.C.; Cademartiri, L. *Nanochemistry: a chemical approach to nanomaterials*, 2nd ed., RSC Publishing, Cambridge, 2009; pp. 335–361.
48. Mayers, B.T.; Liu, K.; Sunderland, D.; Xia, Y. Sonochemical synthesis of trigonal selenium nanowires. *Chem. Mater.* **2003**, *15*, 3852–3858. http://dx.doi.org/10.1021/cm034193b.
49. Jiang, X.; Mayers, B.; Herricks, T.; Xia, Y. Direct synthesis of Se@CdSe nanocables and CdSe nanotubes by reacting cadmium salts with Se nanowires. *Adv. Mater.* **2003**, *15(20)*, 1740–1743. http://dx.doi.org/10.1002/adma.200305737.
50. Gates, B.; Mayers, B.; Wu, Y.; Sun, Y.; Cattle, B.; Yang, P.; Xia, Y. Synthesis and characterization of crystalline Ag_2Se nanowires through a template-engaged reaction at room temperature. *Adv. Funct. Mater.* **2002**, *12*, 679–686. https://doi.org/10.1002/1616-3028(20021016)12:10.
51. Ayele, D.W. A facile one-pot synthesis and characterization of Ag_2Se nanoparticles at low temperature. *Egypt. J. Basic Appl. Sci.* **2016**, *3*, 149–154. http://dx.doi.org/10.1016/j.ejbas.2016.01.002.
52. Kienle, L.; Duppel, V.; Mogwitz, B.; Janek, J.; Kreutzbruck, M.V.; Leineweber, A.; Simon, A. Synthesis–real structure–property: the showcase of silver-rich Ag_2Se. *Cryst. Growth Des.* **2011**, *11*, 2412–2421. https://doi.org/10.1021/cg200167j.
53. Feng, S.; Xu, R. New materials in hydrothermal synthesis. *Acc. Chem. Res.* **2001**, *34(3)*, 239–247. https://doi.org/10.1021/ar0000105.
54. Porter, D.A.; Easterling, K.E. *Phase transformations in metals and alloys*, 2nd. ed.; Chapman and Hall, 1992.
55. Maskaeva, L.N.; Smirnova, Z.I.; Markov, V.F. Assessment of the ability of metal chalcogenides to enter into ion-exchange reactions in aqueous solutions. *Russ. Chem. Bull.* **2014**, *63(7)*, 1515–1522. https://doi.org/10.1007/s11172-014-0629-0.
56. Luo, Y.R. *Comprehensive handbook of chemical bond energies*, 1st ed.; CRC press, Boca Raton, 2007.
57. Beberwyck, B.J.; Surendranath, Y.; Alivisatos, A.P. Cation exchange: a versatile tool for nanomaterials synthesis. *J. Phys. Chem. C* **2013**, *117(39)*, 19759–19770. https://doi.org/10.1021/jp405989z.
58. Yokota, I. On the deviation from the Einstein relation observed for diffusion of Ag^+ ions in α-Ag_2S and others. *J. Phys. Soc. Jpn.* **1966**, *21(3)*, 420–423. http://dx.doi.org/10.1143/JPSJ.21.420.
59. Stehlik, S.; Shimakawa, K.; Wagner, T.; Frumar, M. Diffusion of Ag ions under random potential barriers in silver-containing chalcogenide glasses. *J. Phys. D: Appl. Phys.* **2012**, 45(20), 205304. http://dx.doi.org/10.1088/0022-3727/45/20/205304.
60. Wu, Q.; Liu, X.; Berglund, L.A. FT-IR spectroscopic study of hydrogen bonding in PA6/clay nanocomposites. *Polymer***2002**, *43(8)*, 2445–2449.
61. Krylova, V.; Dukštienė, N. The structure of PA-Se-S-Cd composite materials probed with FTIR spectroscopy. *Appl. Surf. Sci.* **2019**, 470, 462–471. https://doi.org/10.1016/j.apsusc.2018.11.121.

62. Sun, H.; Zhu, X.; Yang, D.; Wangyang, P.; Gao, X.; Tian, H. An economical method for amorphous selenium thick films preparation: e-beam evaporation. *Mater. Lett.* **2016**, *183*, 94–96. http://dx.doi.org/10.1016/j.matlet.2016.07.084i.
63. Tüzüner, S.; Demir, M.M. Dispersion of organophilic Ag nanoparticles in PS-PMMA blends. *Mater. Chem. Phys.* **2015**, *162*, 692–699.
64. Ji, Y.; Yang, X.; Ji, Z.; Zhu, L.; Ma, N.; Chen, D.; Jia, X.; Tang, J.; Cao, Y. DFT-calculated IR spectrum amide I, II, and III band contributions of N-methylacetamide fine components. *ACS Omega* **2020**, *5(15)*, 8572–8578. http://dx.doi.org/10.1021/acsomega.9b04421.
65. Kotkata, M.F.; Masoud, A.E.; Mohamed, M.B.; Mahmoud, E.A. Structural characterization of chemically synthesized CdSe nanoparticles. *Phys. E: Low-Dimens.* **2009**, *41*, 640–645.
66. Sun, Z.B.; Dong, X.Z.; Chen, W.Q.; Shoji, S.; Duan, X.M.; Kawata, S. Two and three dimensional micro/nanostructure pattering of CdS-polymer nanocomposites with a laser interference technique and in situ synthesis. *Nanotechnology* **2008**, *19*, 035611–035619.
67. Helios, K.; Pietraszko, A.; Zierkiewicz, W. Wojtowicz, H.; Michalska, D. The crystal structure, infrared, Raman and density functional studies of bis(2-aminophenyl) diselenide. *Polyhedron* **2011**, *30*, 2466–2472.
68. Sadtler, B.; Demchenko, D.O.; Zheng, H.; Hughes, S.M;. Merkle, M.G.; Dahmen, U.; Wang, L.-W.; Alivisatos, A.P. Selective Facet Reactivity during Cation Exchange in Cadmium Sulfide Nanorods. *J. Am. Chem. Soc.* **2009**, *131*, 5285–5293. http://dx.doi.org/10.1021/ja809854q.
69. Li, Y.C.; Zhong, H.Z.; Li, R.; Zhou, Y.; Yang, C.H.; Li, Y.F. High-yield fabrication and electrochemical characterization of tetrapodal CdSe, CdTe, and $CdSe_xTe_{1-x}$ nanocrystals. *Adv. Funct. Mater.* **2006**, *16*, 1705–1716. https://doi.org/10.1002/adfm.200500678.
70. Ingole, A.R.; Thakare, S.R.; Khati, N.T.; Wankhade, A.V.; Burghate, D.K. Green synthesis of selenium nanoparticles under ambient condition. *Chalcogenide Lett.* **2010**, *7(7)*, 485–489.
71. Surana, K.; Salisu, I.T.; Mehra, R.M.; Bhattacharya, B. A simple synthesis route of low temperature CdSe-CdS core-shell quantum dots and its application in solar cell. *Opt. Mater.* **2018**, *82*, 135–140. https://doi.org/10.1016/j.optmat.2018.05.060.
72. Hegazy, M.A.; Abd El-Hameed, A.M. Characterization of CdSe-nanocrystals used in semiconductors for aerospace applications: Production and optical properties, NRIAG. J. Astron. Geophys. **2014**, *3(1)*, 82–87. http://dx.doi.org/10.1016/j.nrjag.2014.05.002.
73. Pejova, B.; Najdoski, M.; Grozdanov, I.; Dey, S.K. Chemical bath deposition of nanocrystalline (111) textured Ag_2Se thin films. *Mater. Lett*. **2000**, *43*, 269–273. https://doi.org/10.1016/S0167-577X(99)00272-4.
74. Ramezanloo, B.; Molaei, M.; Karimipour, M. Red emissive Ag_2Se quantum dots (QDs) with room-temperature synthesis of both orthorhombic and superionic cubic phases via stirring approach. *J. Lumin.* **2018**, *204*, 419–423. https://doi.org/10.1016/j.jlumin.2018.08.049.
75. Singh, S.; Bharti, A.; Meena, V.K. Green synthesis of multi-shaped silver nanoparticles: optical, morphological and antibacterial properties. *J. Mater. Sci.: Mater. Electron.* **2015**, *26*, 3638–3648. http://dx.doi.org/10.1007/s10854-015-2881-y.
76. Xu, X.; Wang, X.; Zhang, Y.; Li, P. Ion-exchange synthesis and improved photovoltaic performance of CdS/Ag_2S heterostructures for inorganic-organic hybrid solar cells. *Solid State Sci.* **2016**, *61*, 195–200. https://doi.org/10.1016/j.solidstatesciences.2016.10.006.
77. Di, T.; Cheng, B.; Ho, W.; Yu, J.; Tang, H. Hierarchically CdS–Ag_2S nanocomposites for efficient photocatalytic H_2 production. *Appl. Surf. Sci.* **2019**, *470*, 196–204. https://doi.org/10.1016/j.apsusc.2018.11.010.
78. Bubenov, S.S.; Dorofeev, S.G.; Kotin, P.A.; Znamenkov, K.O.; Kuznetsova, T.A. Oleic capped CdSe nanocrystals silver doped in the course of synthesis. *Mendeleev Commun.* **2014**, *24(4)*, 250–252. https://doi.org/10.1016/j.mencom.2014.06.022.
79. Asadpour-Zeynali, K.; Mollarasouli, F. A novel and facile synthesis of TGA-capped CdSe@Ag_2Se core-shell quantum dots as a new substrate for high sensitive and selective methyldopa sensor. *Sens. Actuator B Chem.* **2016**, *237*, 387–399. https://doi.org/10.1016/j.snb.2016.06.116.
80. Ansari, M.Z.; Khare, N. Effect of intrinsic strain on the optical band gap of single phase nanostructured Cu_2ZnSnS_4. *Mater. Sci. Semicond. Process*, **2017**, *63*, 220–226. https://doi.org/10.1016/j.mssp.2017.02.011.
81. Purushotham, E.; Krishna, N.G. Effect of particle size and lattice strain on Debye-Waller factors of Fe_3C nanoparticles. *Bull. Mater. Sci.* **2014**, *37*, 773–778. https://doi.org/10.1007/s12034-014-0005-6.
82. Bhatnagar, A.K.; Venugopal Reddy, K.; Srivastava, V. Optical energy gap of amorphous selenium: effect of annealing. *J. Phys. D: Appl. Phys.* **1985**, *18*, 149–153. http://iopscience.iop.org/0022-3727/18/9/001.
83. Cody, G.D.; Tiedje, T.; Abeles, B.; Moustakas, T.D.; Brooks, B.; Goldstein, Y. Disorder and the optical-absorption edge of hydrogenated amorphous silicon. *J. Phys. Colloques* **1981**, *42*, C4-301−C4-304.
84. Kaiser, O.J. Sandberg, N. Zarrabi et al. A universal Urbach rule for disordered organic semiconductors. *Nat. Commun.* **2021**, *12*, 3988. https://doi.org/10.1038/s41467-021-24202-9.

85. Zhang, C.J.; Mahadevan, S.; Yuan, J.; Ho, J.K.W.; Gao, Y.X.; Liu, W.; Zhong, H.; Yan, H.; Zou, Y.P.; Tsang, S.W.; So, S.K. Unraveling Urbach tail effects in high performance organic.photovoltaics: dynamic vs static disorder, *ACS Energy Lett.* **2022**, *7*, 1971−1979.
86. Ambrosone, G.; Basa, D.K.; Coscia, U.; Fathallah, M. Study on the microstructural and overall disorder in hydrogenated amorphous silicon carbon films. *J. Appl. Phys.* **2008**, *104*, 123520. https://doi.org/10.1063/1.3042242.
87. Rani, S.; Sanghi, S.; Agarwal, A.; Seth, V.P. Study of optical band gap and FTIR spectroscopy of $Li_2O{\cdot}Bi_2O_3{\cdot}P_2O_5$ glasses. *Spectrochim. Acta A* **2009**, *74(3)*, 673–677. https://doi.org/10.1016/j.saa.2009.07.023.
88. Ananth Kumar, R.T.; Chithra Lekha, P.; Sanjeeviraja, C.; Pathinettam Padiyan, D. Evolution of structural disorder using Raman spectra and Urbach energy in $GeSe_{0.5}S_{1.5}$ thin films. *J. Non-Cryst.* **2014**, *405*, 21–26. https://doi.org/10.1016/j.jnoncrysol.2014.08.029.
89. Kabir, H.; Rahman, M.M.; Uddin, K.M.; Bhuiyand, A.H. Structural, morphological, compositional and optical studies of plasma polymerized 2-furaldehyde amorphous thin films. *Appl. Surf. Sci.* **2017,** *423*, 983–994. http://dx.doi.org/doi:10.1016/j.apsusc.2017.06.284.